Article

Patterns

Massive Monte Carlo simulations-guided interpretable learning of two-dimensional Curie temperature

Graphical abstract

Authors

Arnab Kabiraj, Tripti Jain, Santanu Mahapatra

Correspondence

santanu@iisc.ac.in

In brief

Magnetism in two-dimensional materials is an emerging field of science that may revolutionize modern information technology. The magnetic ordering in these materials fluctuates with temperature, which can be estimated by computationally intensive Monte Carlo simulations. Here we develop physically interpretable data-driven models to replace such time-consuming computations while preserving the accuracy at best.

Highlights

- Data-driven models for Curie temperature prediction with exceptional accuracy
- A Curie temperature dataset for a quarter million 2D materials
- Models are interpreted using permutation feature importance and Shapley values
- Pure *ab initio*, automated approach for Curie and Néel temperature prediction

Kabiraj et al., 2022, Patterns *3*, 100625
December 9, 2022
https://doi.org/10.1016/j.patter.2022.100625

CellPress

Please cite this article in press as: Kabiraj et al., Massive Monte Carlo simulations-guided interpretable learning of two-dimensional Curie temperature, Patterns (2022), https://doi.org/10.1016/j.patter.2022.100625

Patterns

CellPress
OPEN ACCESS

Article

Massive Monte Carlo simulations-guided interpretable learning of two-dimensional Curie temperature

Arnab Kabiraj,[1] Tripti Jain,[1] and Santanu Mahapatra[1,2,*]
[1]Nano-Scale Device Research Laboratory, Department of Electronic Systems Engineering, Indian Institute of Science (IISc) Bangalore, Bengaluru 560012, India
[2]Lead contact
*Correspondence: santanu@iisc.ac.in
https://doi.org/10.1016/j.patter.2022.100625

THE BIGGER PICTURE With the rise of artificial intelligence, efforts are being made to develop data-driven models that can replace time-intensive numerical simulations in physical sciences. One such example is the Monte Carlo (MC) method, which relies on a large number of random events and is widely used to simulate the temperature-dependent fluctuations of magnetic ordering of two-dimensional (2D) materials. Here, we develop data-driven models that can perform the MC process-based Curie temperature calculation with exceptional accuracy in the blink of an eye. We achieve such performance by coupling the learning to the data-generation process and conducting a massive amount of MC simulations accelerated by a bisection-technique-based search. Our models could aid in the rapid discovery of beyond-room-temperature 2D magnetism, a rapidly emerging field in nanoscience and technology.

Proof-of-Concept: Data science output has been formulated, implemented, and tested for one domain/problem

SUMMARY

Monte Carlo (MC) simulation of the classical Heisenberg model has become the de facto tool to estimate the Curie temperature (T_C) of two-dimensional (2D) magnets. As an alternative, here we develop data-driven models for the five most common crystal types, considering the isotropic and anisotropic exchange of up to four nearest neighbors and the single-ion anisotropy. We sample the 20-dimensional Heisenberg spin Hamiltonian and conceive a bisection-based MC technique to simulate a quarter of a million materials for training deep neural networks, which yield testing R^2 scores of nearly 0.99. Since 2D magnetism has a natural tendency toward low T_C, learning-from-data is combined with data-from-learning to ensure a nearly uniform final data distribution over a wide range of T_C (10–1,000 K). Global and local analysis of the features confirms the models' interpretability. We also demonstrate that the T_C can be accurately estimated by a purely first-principles-based approach, free from any empirical corrections.

INTRODUCTION

A new horizon in nanotechnology has opened up with the experimental demonstration of low-temperature ferromagnetism in two-dimensional (2D) materials CrI_3 and $Cr_2Ge_2Te_6$.[1,2] The presence of long-range antiferromagnetic order was also detected in atomically thin $FePS_3$,[3] firmly establishing the fact that magnetic order can indeed be sustained in 2D at finite temperatures. Mermin and Wagner argued in their famous work that an isotropic Heisenberg model must enforce the absence of long-range magnetic order in 2D at positive finite temperatures.[4] However, the significant magnetocrystalline anisotropy of these 2D materials overcomes the Mermin-Wagner constraint, making it feasible to detect even beyond-room-temperature ferromagnetism in monolayer VSe_2 (both 1T[5] and 2H[6] phases) and $MnSe_x$ more recently.[7] Magnetism in two dimensions is attracting tremendous technological importance, since it can potentially revolutionize fields such as spintronics,[8] valleytronics,[9] sensing, and memory technologies.[10]

In parallel with experimental efforts,[11] *in silico* screening of the vast material space based on a combination of density functional theory (DFT) and Monte Carlo (MC) simulation has been an essential tool to predict the magnetic properties of 2D materials.[12–17] It is especially important for the prediction of

ferromagnetic (FM) or antiferromagnetic (AFM) to paramagnetic (PM) transition temperature, known as the Curie or Néel temperature (T_C or T_N), which is probably the most vital property in the context of practical usage. Fitting the DFT-calculated energies and spin values to an anisotropic Heisenberg model and performing a classical MC (where the spins are treated as classical three-dimensional vectors) based on this model usually yields an accurate prediction of the transition temperature.[17–20] On the other hand, semiclassical or full quantum methods such as renormalized spin-wave (RNSW), Green's function, or path-integral quantum MC have also been demonstrated to predict accurate values of the transition temperature.[21,22] However, in addition to the prediction accuracy, the simplicity of the classical MC of the anisotropic Heisenberg model has made it a common choice for determining the T_C (for FM) or T_N (for AFM) of 2D magnets.

Nevertheless, the relatively "simple" classical MC can become computationally highly expensive for high-throughput studies, where many materials need to be rapidly screened based on their T_C.[20,22] Moreover, the accuracy of the MC process strongly depends on the system size and number of steps. Extensive efforts have therefore been made to replace the MC process with a much less expensive but similarly accurate method, such as developing an analytical formula of the T_C.[18,20,22,23] Although these formulas are shown to be accurate for a few cases, they can be heavily approximated, considering only the first or second nearest neighbor interactions and sometimes even ignoring the effect of the single-ion anisotropy. Furthermore, these expressions are limited to only a few lattice types (square, honeycomb, and hexagonal). At the same time, the underlying DFT-based process to calculate the magnetic parameters (spin, isotropic and anisotropic exchange, and single-ion anisotropy), which act as inputs to the MC engine, is also highly critical. The parameter values depend greatly on the exchange-correlation (XC) functional used and other empirical corrections such as Hubbard U and Hund J in the case of DFT + U and the percentage of Hartree-Fock exchange in the case of hybrid functionals. The main disadvantage of using such empirical parameters is that they are strongly system dependent, and thus their values should be recalibrated for each system,[19,24] which again is unsuitable for high-throughput screening purposes.

With the increased abundance of materials data, both experimental and computational, machine learning (ML) has become extremely relevant in materials science and chemistry.[25–28] In our previous work, we developed an FM/AFM classifier and a T_C predictor directly from the crystal structure.[19] Since then, innovative ML models with relevant features have been developed to predict the magnetic ground state of 2D materials accurately,[29] and an active-learning-based model with a universal magnetic representation has been proposed to precisely screen for high T_C 2D materials even with scarce data by predicting the magnetic configurational energy difference.[30] Furthermore, sure independence screening and sparsifying operator (SISSO) analysis was used to generate a simple expression of T_C from crystal descriptors of 79 materials with moderate success,[31] perhaps because of the small dataset. Despite these advances, a generalized analytical expression or an ML model that can accurately predict the T_C of 2D magnets from the DFT-obtained magnetic parameters without performing the costly MC process is still lacking. Also, there is no standard one-size-fits-all empirical correction-free true first-principles-based methodology that can predict the magnetic properties of 2D materials accurately.

In this work, we first propose a generalized anisotropic Heisenberg Hamiltonian that can deal with the easy axis aligning in any of the three principal directions, considers both isotropic and anisotropic exchanges up to the fourth nearest neighbors, and also the single-ion or on-site anisotropy. Incorporating this Hamiltonian, we develop an automated computational workflow that can predict the magnetic properties, including T_C or T_N, of any 2D material, starting from its crystal structure information. We show that when the DFT calculations are performed with a newly developed meta-generalized gradient approximation (meta-GGA)-based regularized-restored strongly constrained and appropriately normed (r^2SCAN)[32] XC functional, the workflow-predicted T_C or T_N of 2D materials consistently match the experimentally reported values without any empirical corrections such as Hubbard U or Hund J.

Next, armed with the physical constraints, we sample the 20-dimensional input parameter space of the MC process near-uniformly. We then perform a massive amount of MC simulations on these random data and use a bisection method to precisely estimate the T_C. Ultimately, we generate about 50,000 data points for each crystal type, and the final ML models are trained on these data. The resulting models exhibit a mean absolute error (MAE) of 11.85–20.36 K and an R^2 score of 0.983–0.994 on the unseen test datasets, which can be considered excellent. Furthermore, we show that the model performs exceptionally well by accurately predicting T_C of real experimental or computationally predicted 2D materials. Both global and local interpretability analyses are performed on the models, and valuable insights are drawn into the contribution of each term of the Hamiltonian to the T_C. Our work can significantly accelerate the high-throughput discovery of 2D FM materials.

RESULTS AND DISCUSSION

Spin Hamiltonian and fitting

We begin by defining our generalized anisotropic Heisenberg spin Hamiltonian below.

$$
\begin{aligned}
H = & -\frac{1}{2}J_1\sum_{i,j}\boldsymbol{S}_i.\boldsymbol{S}_j - \frac{1}{2}J_2\sum_{i,k}\boldsymbol{S}_i.\boldsymbol{S}_k - \frac{1}{2}J_3\sum_{i,l}\boldsymbol{S}_i.\boldsymbol{S}_l - \frac{1}{2}J_4\sum_{i,m}\boldsymbol{S}_i.\boldsymbol{S}_m \\
& -\frac{1}{2}K_{1x}\sum_{i,j}S_i^x\,S_j^x - \frac{1}{2}K_{1y}\sum_{i,j}S_i^y\,S_j^y - \frac{1}{2}K_{1z}\sum_{i,j}S_i^z\,S_j^z \\
& -\frac{1}{2}K_{2x}\sum_{i,k}S_i^x\,S_k^x - \frac{1}{2}K_{2y}\sum_{i,k}S_i^y\,S_k^y - \frac{1}{2}K_{2z}\sum_{i,k}S_i^z\,S_k^z \\
& -\frac{1}{2}K_{3x}\sum_{i,l}S_i^x\,S_l^x - \frac{1}{2}K_{3y}\sum_{i,l}S_i^y\,S_l^y - \frac{1}{2}K_{3z}\sum_{i,l}S_i^z\,S_l^z \\
& -\frac{1}{2}K_{4x}\sum_{i,m}S_i^x\,S_m^x - \frac{1}{2}K_{4y}\sum_{i,m}S_i^y\,S_m^y - \frac{1}{2}K_{4z}\sum_{i,m}S_i^z\,S_m^z \\
& -A_x\sum_i\left(S_i^x\right)^2 - A_y\sum_i\left(S_i^y\right)^2 - A_z\sum_i\left(S_i^z\right)^2
\end{aligned}
\qquad \text{(Equation 1)}
$$

Please cite this article in press as: Kabiraj et al., Massive Monte Carlo simulations-guided interpretable learning of two-dimensional Curie temperature, Patterns (2022), https://doi.org/10.1016/j.patter.2022.100625

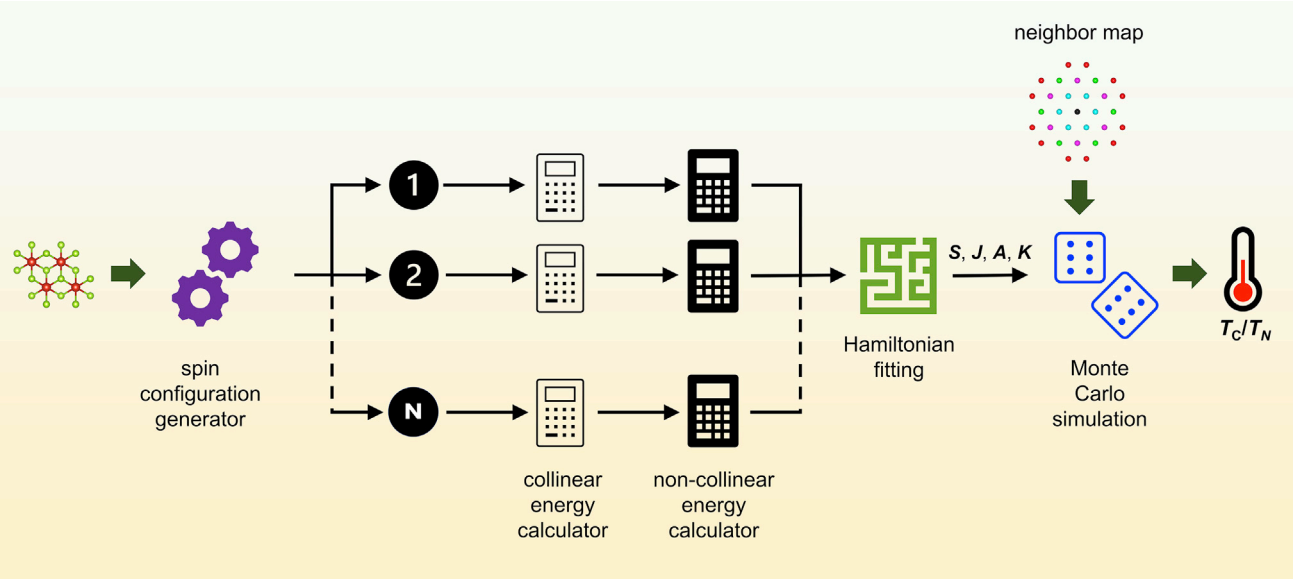

Figure 1. Schematic of the automated workflow for determining the transition temperature of 2D magnets

Here, J_1, J_2, J_3, and J_4 terms represent isotropic exchanges with the first, second, third, and fourth nearest magnetic neighbors, respectively. $\boldsymbol{S}_i$ represents the spin of the site in question, and $\boldsymbol{S}_j$, $\boldsymbol{S}_k$, $\boldsymbol{S}_l$, and $\boldsymbol{S}_m$ are the spins of sites at the first, second, third, and fourth nearest magnetic neighbor shells. These spins are all 3D vectors, and the individual spin components are represented as S_n^d, where $n = i, j, k, l$ and $d = x, y, z$. The K_{pd} terms represent the anisotropic exchange for neighbor shell p (p = 1, 2, 3, 4) and direction d ($d = x, y, z$). The A_d terms represent the single-ion anisotropy for direction d. Note that the ½ factor for the exchange terms is there to counter the effect of double counting. This Hamiltonian covers all the essential interactions commonly exhibited by 2D magnets. However, for simplicity, we exclude complex interactions such as antisymmetric or Dzyaloshinskii-Moriya interaction exchange, which is anyway not expected to exist in centrosymmetric materials, and magnetic dipole-dipole interactions, which usually do not significantly affect the transition temperature. We also assume the material to be uniform, i.e., each magnetic site in the material to possess an equal magnitude of spin, S. We end up with 20 independent material parameters: S, J_1, J_2, J_3, J_4, K_{1x} , K_{1y}, K_{1z}, K_{2x}, K_{2y}, K_{2z}, K_{3x}, K_{3y}, K_{3z}, K_{4x}, K_{4y}, K_{4z}, A_x, A_y, and A_z. We note that only the out-of-plane components of the anisotropy parameters, i.e., K_{pz} and A_z, calculated relative to their in-plane counterparts, are enough to represent magnetism in 2D materials with an easy plane or out-of-plane easy axis, but the inclusion of the in-plane anisotropy components ensures that the Hamiltonian mentioned above can represent magnetism of materials with an easy axis in either of the x, y, or z directions.

There are, however, practical problems in extracting the y component of the anisotropy parameters, i.e., K_{py} and A_y, for crystals with non-orthogonal unit cell axes, such as hexagonal unit cells. For these cases, we adopt an XXZ model, i.e., we assume in-plane isotropy and make $K_{px} = K_{py}$ and $A_x = A_y$. This is usually a reasonable approximation for hexagonal 2D magnets because the in-plane anisotropy is usually much weaker compared with the out-of-plane anisotropy.[18,23,33] The XXZ model is also assumed in the case of materials with square unit cells for obvious reasons. The XYZ model is adequately implemented for rectangular unit cells where it is most relevant.

Fitting the DFT data to 20 parameters at once is not an easy feat, and we implement this in a graded manner. First, along with S, the isotropic J_p terms are fitted to the energies of different collinear FM and AFM magnetic configurations. Next, the effect of spin-orbit coupling is turned on, and the magnetization axis is aligned to the x (y) and z directions for the FM and various AFM magnetic configurations. The difference between the collinear and non-collinear (magnetism aligned to x, y, or z) total energies are assumed to be entirely contributed by the anisotropic exchange and on-site anisotropy terms for those specific directions, and a further fitting procedure is performed to obtain these. This way, the equations for isotropic and direction-dependent anisotropic terms become decoupled and thus become easier to solve.

Validation with experimental data

Incorporating the aforementioned Hamiltonian, we develop an automated workflow, which significantly improves upon our previous work.[19] Compared with the earlier version, the upgraded workflow takes into account the effect of anisotropic exchanges and also works seamlessly with AFM materials. Starting only from the crystal structure of a 2D material, the developed code can automatically generate symmetry-constrained possible FM and AFM configurations, calculate their collinear and non-collinear energies with the magnetic moments oriented in the x (y) and z directions using DFT, then perform a fitting to obtain the magnetic parameters of the Hamiltonian and finally perform an automatic neighbor mapping of a large supercell followed by a series of MC simulations of the model to determine the transition temperature. The whole workflow is depicted pictorially in Figure 1.

The parameter values and, in turn, the transition temperature and even the magnetic ground state are entirely dependent on the DFT calculators. It is well known that local or semilocal

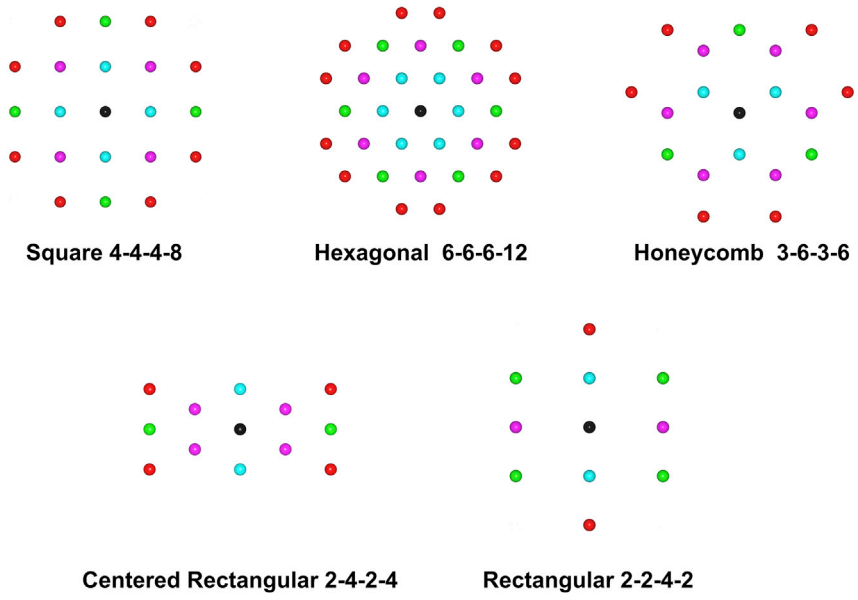

Figure 2. Different crystal types and their neighbor coordination

Only magnetic sites are shown. The black site is the reference, and the blue, magenta, green, and red sites make up the first, second, third, and fourth nearest neighboring shells, respectively.

DFT is unable to predict the accurate energetics when the system in question contains elements with localized and open d or f orbitals (which is the case for magnetic materials). Usually, a combination of Hubbard U and Hund J correction is therefore required for these orbitals to counter the effect of the self-interaction error. However, the U/J values are empirical and strongly material dependent.[19,24] Recently developed meta-GGA XC functional SCAN[34] is a semilocal density functional that fulfills all known constraints that the exact density functional must satisfy. It has been demonstrated that SCAN is superior to most gradient-corrected functionals and can even deal with strongly correlated magnetic materials without any empirical corrections.[35–37] However, SCAN is known to be vulnerable to numerical instabilities, and an upgraded version of this functional, r^{2}SCAN, was recently introduced that is shown to match the accuracy of the parent SCAN functional but with much enhanced numerical efficiency and accuracy with low-cost computational settings.[32] We thus identify the r^{2}SCAN functional as the ideal XC functional to be employed for empirical-correction-free accurate DFT calculators despite it being more computation extensive than GGA + U. We initially test this workflow on experimentally synthesized and characterized FM materials CrI_3, $CrBr_3$, and $CrCl_3$, and AFM material $FePS_3$. The workflow predicts their T_C (T_N in the case of AFM $FePS_3$) to be 53.52 K, 31.43 K, 19.5 K, and 131.32 K, respectively, which are remarkably close to the experimentally determined values (45 K,[1] 27–34 K,[38,39] 16 K (bilayer),[38,40] and 118 K[3]). After developing the ML models, we further test our workflow on a host of real materials and show that our workflow and ML models consistently predict the T_C accurately.

Sampling the input space and data generation

Although our workflow can handle both FM and AFM materials, we focus only on FM material for greater technological importance while developing the ML model. Figure 2 shows the most common five types of 2D magnetic crystals and their magnetic neighbor distribution up to the fourth nearest neighbor. The four numbers represent coordination numbers for the respective neighbor shells. For instance, the representation 2-2-4-2 means for this particular crystal type, each magnetic site is surrounded by two magnetic nearest neighbors, two second nearest neighbors, four third nearest neighbors, and two fourth nearest neighbors. From here on, we would identify these crystal types by their unique format CN_1-CN_2-CN_3-CN_4, where CN_p (p = 1, 2, 3, 4) is the magnetic coordination number of the p^{th} neighboring shell. The experimentally studied materials CrI_3, $CrBr_3$, $CrCl_3$, and $Cr_2Ge_2Te_6$ all fall under the crystal type 3-6-3-6.

Usually in materials science, the main obstacle to developing accurate ML models is the lack of data.[25,41] For properly generating the inputs for the data, we decide to sample the 20-dimensional input parameter space as uniformly as possible. However, these inputs must be generated with adequate physical constraints. Ideally, the magnetic moment of a magnetic site in a material must be 1, 2, 3, 4, or 5 μ_B, depending on the number of unpaired electrons in the site's (hybridized) d orbital. However, it can go up to 6 μ_B depending on the hybridization. This implies that the value of S must become half of these integers, i.e., $S \in [0.5, 1, 1.5, 2, 2.5, 3]$. When choosing S, we pick a value from this discrete set uniformly and randomly. Similarly, we choose the J_p values from the continuous interval of -20 meV/link to 20 meV/link. In our experience, the J_p values of the real materials usually fall in this range. After generating the S and J_p values, the condition $\sum_{p=1}^{4} CN_p J_p > 0$ is checked, which ensures FM behavior, and the values are not accepted unless they satisfy this criterion. We further note that among the five crystal types, we use XXZ model for 4-4-4-8, 6-6-6-12, and 3-6-3-6, while the XYZ model is employed for 2-4-2-4 and 2-2-4-2. Again, from experience, A_z is chosen from the continuous range of 0 to 300 meV/magnetic atom, and A_x (and A_y for the XYZ model) are selected from the range $A_z - 1 < A_x\,(A_y) < A_z + 1$ as long as $A_x\,(A_y) \geq 0$. It is worth noting that because of our chosen spin Hamiltonian and unique fitting procedure, the values of the A_d terms are absolute and, therefore, can be quite large. However, only their relative values would matter in the MC process, which is no more than 1 meV/atom. Finally, the K_{pd} values are independently chosen from the range -2 meV/link to 2 meV/link.

After generation, this initial input set is subjected to MC simulations. 2D materials exhibit a natural tendency for low T_C, and this is indeed reflected in the MC simulations. Most of the ($\approx$97%) initial inputs produce T_C predominantly below the lower

Please cite this article in press as: Kabiraj et al., Massive Monte Carlo simulations-guided interpretable learning of two-dimensional Curie temperature, Patterns (2022), https://doi.org/10.1016/j.patter.2022.100625

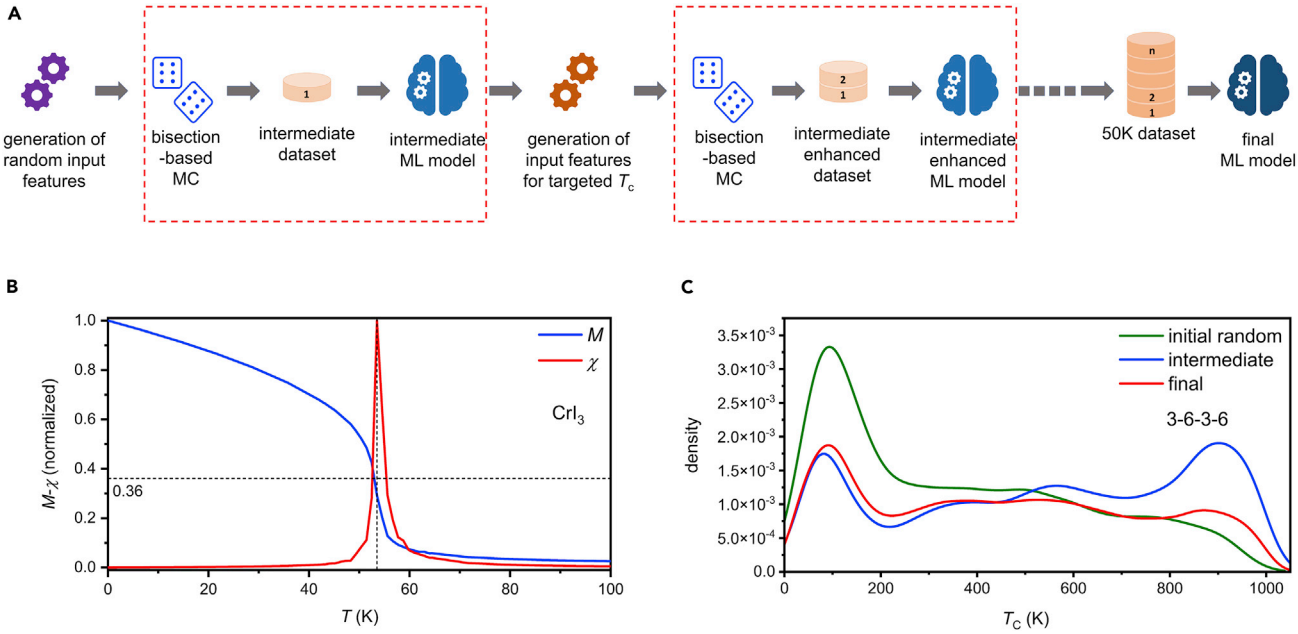

Figure 3. Details of data generation

(A) Schematic of the coupled data-generation-model-training process.

(B) Validation of the empirical magnetism-based definition of T_C for the case of CrI_3.

(C) Evolution of the T_C distribution of the generated data for different batches.

limit (10 K). A concept of data generation using intermediate ML models is introduced to address this problem. The data generation-ML training coupled pipeline is schematically shown in Figure 3A. The inputs from the first batch are truly random except for the imposed physical constraints. The resulting data are then used to train an initial deep neural network (DNN) model. While generating the next batch of input parameters, in addition to the previously mentioned physical constraints, it is ensured that the DNN predicts the T_C of these inputs to be in our desired range. The resulting data are then again used to train another intermediate DNN, which is expected to be more accurate than its predecessor. This process is repeated until we obtain ≈50,000 data points for each crystal type, then a 0.9:0.1 train-test split (see experimental proceduress) is performed on these data, and final DNNs are adequately trained and tested.

The massive MC process requires domain knowledge-based engineering to determine the T_C with enough precision in the shortest possible time. To achieve this feat, we devise a bisection-based T_C-searching technique. The MC engine is provided with a lower and an upper limit of T_C to search in between. For the initial batch, this range for all points is 10–1,000 K, and for ML-guided subsequent batches, this range is decided to be $T_{C-ML}/2$ to $3T_{C-ML}/2$. The MC-powered search for T_C has been performed in two stages. In the first stage, the entire range is divided into six equally spaced points; for the initial batch, these are 10 K, 200 K, 400 K, 600 K, 800 K, and 1,000 K. The MC then is run for these specific temperatures, and it is observed at what point the magnetism has fallen close to zero. If the normalized average magnetic moment (M) was close to 1 (>0.6) at point T_n K but falls below 0.1 at point T_{n+1} K, these two temperature values are further passed down to another MC-based search engine, the second stage that employs a six-step bisection process to find the exact point of transition. Usually, we define the transition temperature as the temperature where the magnetic susceptibility (χ) peaks, but this is difficult to identify by a bisection search. Instead, we search for the temperature where M reaches an empirical value of 0.36. This value was decided upon after rigorous testing on random and real materials data. In Figure 3B, we show that for CrI_3, this definition of T_C yields an almost exact match with its classical χ peak-based counterpart. An oscillation in M values is observed for a few input combinations despite running each MC for 1.5×10^5 steps (MCS), and these points are discarded.

The importance of the bisection process in accurately determining the T_C is worth emphasizing. Locating the T_C with a full linear sampling scheme and reasonable accuracy in the large temperature range can be highly tedious and might require susceptibility evaluation of about 100 temperature points in total. Our employed combination of linear sampling and bisection scheme can reach the same accuracy with a mere 12-point temperature evaluation, accelerating the data-generation process greatly.

Inevitably, the "curse" of low T_C follows us into these valid datasets despite the T_C being in the desired range, as evident from Figure 3C. In the initial batch, the T_C distribution of the data exhibits a massive peak at around 70 K compared with the mid- and high-temperature regions. For ideal training, we would like to have a nearly uniform distribution. To address this problem, targeted inputs are generated using the intermediate ML models in the subsequent batches to increase the T_C density in high-temperature regions. From Figure 3C, it can be seen that after a while we end up with a double-peaked intermediate

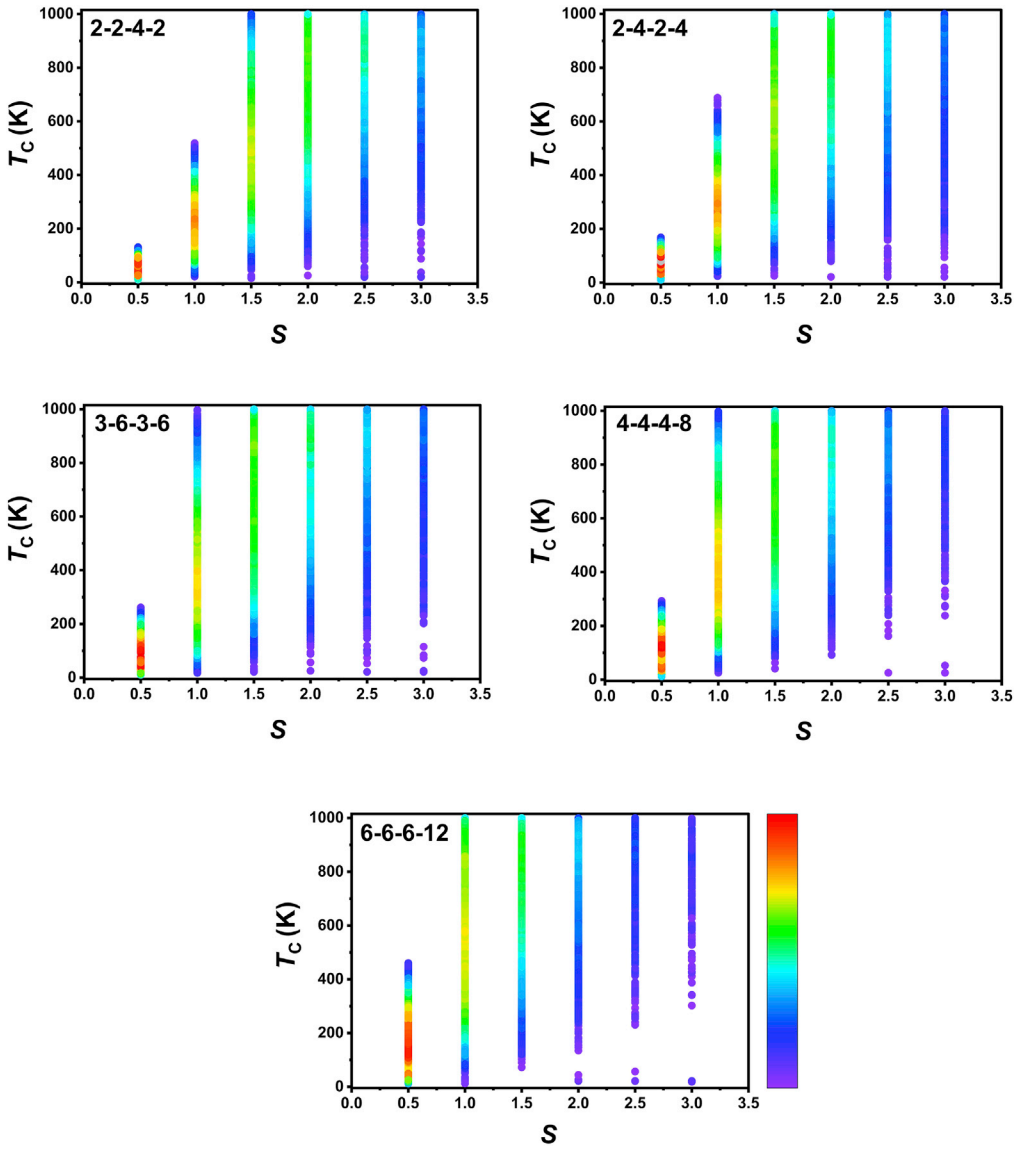

Figure 4. Distribution of Curie temperature with respect to spin

The blue-purple end of the color bar represents low density, whereas the red end represents high density.

distribution with peaks at both low and high temperatures. To rectify this, targeted inputs predicted to produce T_C in the mid-temperature regions are subsequently generated. This process is repeated until we achieve a data distribution satisfactorily close to a uniform distribution.

Figure 4 shows the distribution of T_C with respect to probably the most important material property, S, for all lattice types. The effect of coordination numbers is clearly visible here; the higher the coordination, the more frequently the T_C tends to be in the higher region for the same values of S. The full distribution of all 20 input features and T_C for all lattice types is depicted in Figures S1–S5.

Accuracy of the models

A pictorial depiction of the performance of the final DNN models on the unseen ~5,000 test data points (for each crystal type) is shown in Figure 5. An MAE of 11.85–20.36 K and R^2 score of 0.983–0.994 are recorded, which can be considered accurate enough considering the large range of the data. As discussed before, owing to the relative abundance of data at low temperatures, the predictions are relatively more accurate there.

After testing the model accuracy on hypothetical data, we examine the predictive prowess of the result produced by our DFT-MC-based workflow for real experimental or computationally predicted materials. Especially to the best of our knowledge, no square 2D FM materials have yet been experimentally studied, and we can test our model only on computationally predicted materials. For other cases, too, experimentally studied materials are supplemented with computationally predicted materials of our choosing to test the ML models' accuracy thoroughly. The details are presented in Table 1. Our computational pipeline and ML models predict the T_C reasonably accurately for the cases where experimental data are available. For the cases

Please cite this article in press as: Kabiraj et al., Massive Monte Carlo simulations-guided interpretable learning of two-dimensional Curie temperature, Patterns (2022), https://doi.org/10.1016/j.patter.2022.100625

CellPress
OPEN ACCESS

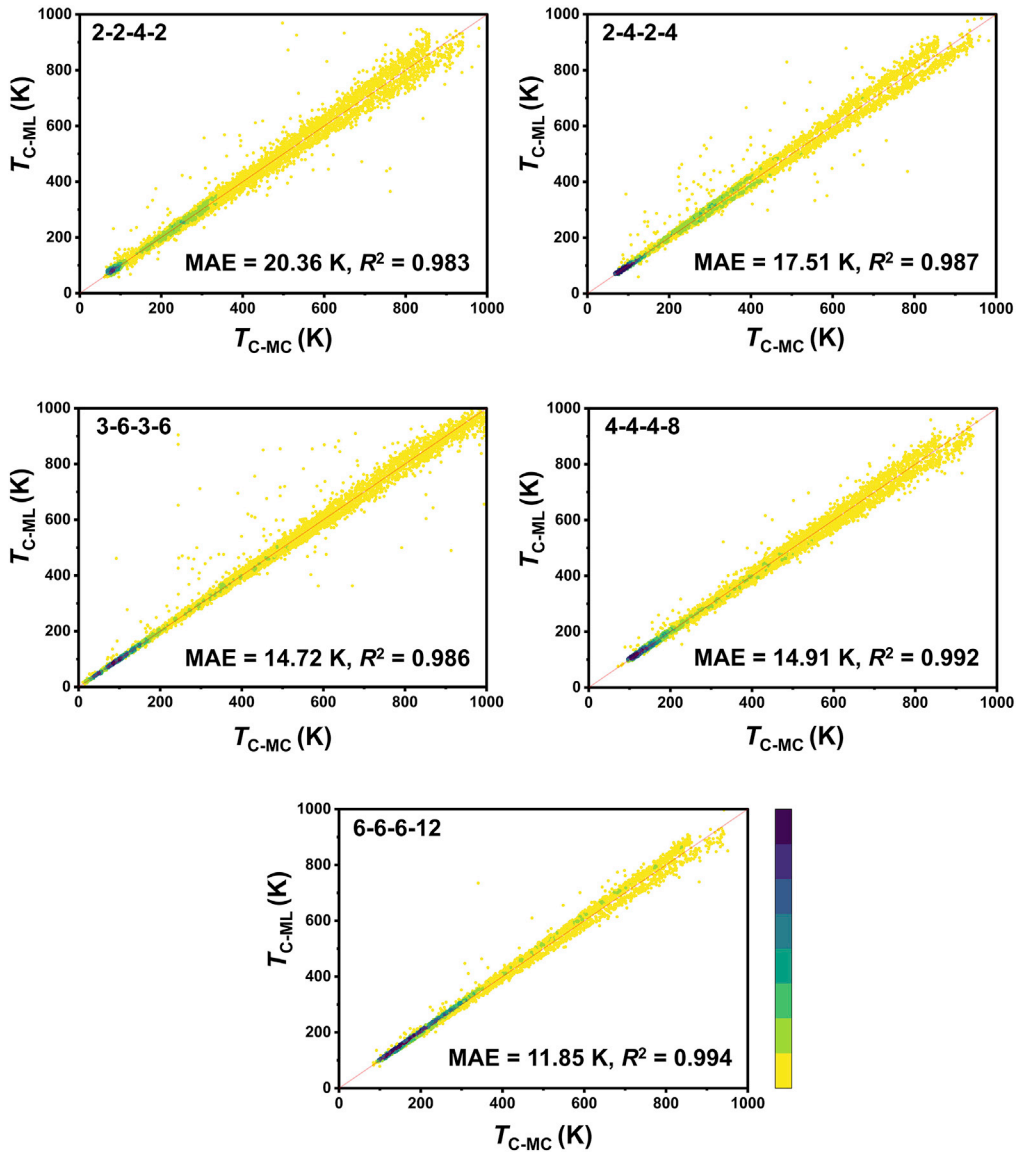

Figure 5. Performance of the ML models on unseen test data

The yellow end of the color bar represents low density, while the dark purple end represents high density.

where it is not available, we have referred to relevant computational studies whenever available. For both 1T and 2H phases of monolayer VSe_2, the T_C values are underpredicted. This could be a systemic problem with r^{2}SCAN and element V. Also, the DFT calculations are performed on freestanding monolayers, and substrate effects have been ignored. The substrate-induced effects, such as charge transfer and strain, can also contribute to this discrepancy.[5,42] These materials also show charge density wave (CDW) nature at low temperatures that can couple with the magnetism, affecting the prediction. There is controversy around the claim of room-temperature ferromagnetism of monolayer 1T-VSe_2.[6] Nevertheless, our methodology reproduces the high-temperature FM nature of both the 1T and 2H phases of VSe_2. We also note that the workflow fails to predict the T_C of 1T-$CrTe_2$ accurately, albeit there is no report as yet of measurement of T_C at the monolayer/bilayer. Furthermore, the T_C of 2D $CrTe_2$ exhibits strong anomalous layer dependence.[43] For three 1T materials, VSe_2, VTe_2, and $CrTe_2$, the atomic magnetic moments turn out to be fractional from DFT, and in turn the values of S fall in between the discrete values with which our ML model was trained. This leads to extremely unreasonable ML predictions for these cases. The solution to this problem can be a simple refitting of the Hamiltonian, whereby the magnetic moment is forced to be the nearest integer and the other parameter values are adjusted automatically. The refitting process does not effectively change the MC prediction of the T_C but it enables the ML prediction to regain its accuracy. Although the ML models seem to be failing with interpolating values of S, they retain their accuracy when tested with out-of-range values of J_1 or A_d. For the cases of CrO_2_P-4m2, VSe_2-2H, VSi_2N_4, and VSi_2P_4, the

CellPress OPEN ACCESS

Please cite this article in press as: Kabiraj et al., Massive Monte Carlo simulations-guided interpretable learning of two-dimensional Curie temperature, Patterns (2022), https://doi.org/10.1016/j.patter.2022.100625

Table 1. Performance of DFT-MC workflow and ML models on real experimental and computationally predicted materials

Material	S	J_1 (meV/link)	J_2 (meV/link)	J_3 (meV/link)	J_4 (meV/link)	K_{1x} (meV/link)	K_{1y} (meV/link)	K_{1z} (meV/link)	K_{2x} (meV/link)	K_{2y} (meV/link)	K_{2z} (meV/link)	K_{3x} (meV/link)	K_{3y} (meV/link)	K_{3z} (meV/link)	K_{4x} (meV/link)	K_{4y} (meV/link)	K_{4z} (meV/link)	A_x (meV/atom)	A_y (meV/atom)	A_z (meV/atom)	Crystal type	$T_{C\text{-}DFT\text{-}MC}$ (K)	$T_{C\text{-}ML}$ (K)	$T_{C\text{-}expt}$ (K)
$CrPS_4$	1.50	5.93	0.07	0.67	−1.20	−0.21	−0.21	−0.21	−0.01	−0.01	−0.01	−0.01	−0.01	−0.01	0.05	0.05	0.05	6.72	6.72	6.73	2-2-4-2	46.65	32.90	23 (monolayer), Son et al.[44]
$CrPSe_4$	1.50	7.12	0.08	1.14	−0.88	−0.56	−0.56	−0.56	−0.04	−0.04	−0.03	−0.11	−0.11	−0.12	0.15	0.15	0.16	40.05	40.05	40.05	2-2-4-2	50.00	57.04	N/A, Deng et al.[45]
$CrPTe_4$	1.47	9.04	0.52	3.66	−0.63	0.37	0.37	0.73	−0.09	−0.09	0.33	−0.23	−0.23	−0.33	−0.18	−0.18	−0.15	198.45	198.45	198.02	2-2-4-2	147.83	141.17	N/A, Deng et al.[45]
CrSBr	1.50	4.58	6.21	4.22	0.04	−0.23	−0.20	−0.21	−0.03	−0.03	−0.03	−0.07	−0.08	−0.08	0.05	0.05	0.05	16.91	16.88	16.87	2-4-2-4	205.33	214.57	146 (monolayer), Lee et al.[46]
CrSeBr	1.50	3.10	6.61	2.26	0.03	−0.46	−0.40	−0.41	0.02	0.01	0.00	−0.26	−0.26	−0.26	0.14	0.15	0.15	24.76	24.71	24.69	2-4-2-4	174.08	179.36	N/A, Wang et al.[47]
$Cr_2Ge_2Te_6$	1.50	6.64	0.04	0.33	0.00	−0.31	−0.31	−0.01	0.02	0.02	0.01	0.12	0.12	−0.01	0.00	0.00	0.00	136.27	136.27	136.05	3-6-3-6	67.29	78.87	66 (bilayer), Gong et al.[2]
$CrBr_3$	1.50	2.39	0.23	−0.05	0.00	−0.37	−0.37	−0.37	0.01	0.01	0.01	−0.04	−0.04	−0.02	0.00	0.00	0.00	40.26	40.26	40.31	3-6-3-6	31.43	32.23	27–34 (monolayer), Kim et al. and Zhang et al.[38,39]
$CrCl_3$	1.50	1.82	0.13	−0.04	0.00	−0.21	−0.21	−0.21	−0.01	−0.01	−0.01	0.00	0.00	0.00	0.00	0.00	0.00	7.13	7.13	7.14	3-6-3-6	19.50	24.15	16 (bilayer), Kim et al.[38]
CrI_3	1.50	3.04	0.48	−0.05	0.00	−0.57	−0.57	−0.37	0.01	0.01	0.02	0.12	0.12	−0.03	0.00	0.00	0.00	173.52	173.52	173.64	3-6-3-6	53.52	49.42	45 (monolayer), Huang et al.[1]
CrO_2_P-4m2	1.00	65.22	0.07	5.71	−2.79	0.16	0.16	0.13	0.02	0.02	0.04	0.16	0.16	0.10	0.02	0.02	0.03	9.86	9.86	9.89	4-4-4-8	429.17	473.96	N/A, Kabiraj et al.[19]
MnO_2_P-4m2	1.50	31.08	−3.87	−10.74	2.11	0.06	0.06	0.10	−0.08	−0.08	−0.07	0.25	0.25	0.22	−0.19	−0.19	−0.20	4.53	4.53	4.73	4-4-4-8	100.83	126.30	N/A, Kabiraj et al.[19]
$CrTe_2$	1.30	0.56	1.34	−0.76	0.00	0.36	0.36	0.24	0.09	0.09	0.14	0.05	0.05	−0.15	0.00	0.00	0.00	135.62	135.62	135.16	6-6-6-12	40.58	−22.52	213 (few layers), Meng et al.[43]
$CrTe_2$_refit_high	1.50	0.42	1.01	−0.57	0.00	0.27	0.27	0.18	0.06	0.06	0.10	0.04	0.04	−0.11	0.00	0.00	0.00	101.86	101.86	101.51	6-6-6-12	40.42	45.63	213 (few layers), Meng et al.[43]
$CrTe_2$_refit_low	1.00	0.95	2.27	−1.28	0.00	0.61	0.61	0.41	0.15	0.15	0.24	0.08	0.08	−0.25	0.00	0.00	0.00	229.19	229.19	228.40	6-6-6-12	41.57	39.46	213 (few layers), Meng et al.[43]

(*Continued on next page*)

Please cite this article in press as: Kabiraj et al., Massive Monte Carlo simulations-guided interpretable learning of two-dimensional Curie temperature, Patterns (2022), https://doi.org/10.1016/j.patter.2022.100625

Table 1. *Continued*

Material	S	J_1 (meV/link)	J_2 (meV/link)	J_3 (meV/link)	J_4 (meV/link)	K_{1x} (meV/link)	K_{1y} (meV/link)	K_{1z} (meV/link)	K_{2x} (meV/link)	K_{2y} (meV/link)	K_{2z} (meV/link)	K_{3x} (meV/link)	K_{3y} (meV/link)	K_{3z} (meV/link)	K_{4x} (meV/link)	K_{4y} (meV/link)	K_{4z} (meV/link)	A_x (meV/atom)	A_y (meV/atom)	A_z (meV/atom)	Crystal type	$T_{C\text{-}DFT\text{-}MC}$ (K)	$T_{C\text{-}ML}$ (K)	$T_{C\text{-}expt}$ (K)
$MnSe_2$	1.50	7.44	0.41	−2.04	0.00	−0.14	−0.14	−0.08	0.11	0.11	0.11	0.01	0.01	0.03	0.00	0.00	0.00	24.31	24.31	24.24	6-6-6-12	91.00	124.18	>300 (thick $MnSe_x$), O'Hara et al.[7]
VSe_2-1T	0.56	21.90	17.79	14.55	0.00	0.13	0.13	−0.45	−0.32	−0.32	0.20	0.06	0.06	0.30	0.00	0.00	0.00	161.98	161.98	161.35	6-6-6-12	271.50	938.19	>300 (monolayer), Bonilla et al.[5]
VSe_2-1T_refit	0.50	27.04	21.96	17.96	0.00	0.16	0.16	−0.56	−0.40	−0.40	0.25	0.08	0.08	0.37	0.00	0.00	0.00	199.98	199.98	199.20	6-6-6-12	280.00	274.35	>300 (monolayer), Bonilla et al.[5]
VSe_2-2H	0.50	141.99	−5.02	−7.26	0.00	0.74	0.74	0.08	−0.49	−0.49	−0.38	−0.21	−0.21	−0.23	0.00	0.00	0.00	194.13	194.13	194.25	6-6-6-12	332.38	339.44	430 (few layers), Wang et al.[6]
VSi_2N_4	0.50	120.45	9.36	−1.59	0.00	0.43	0.43	0.29	0.03	0.03	0.06	0.13	0.13	0.13	0.00	0.00	0.00	30.11	30.11	30.16	6-6-6-12	402.00	388.40	N/A, Akanda and Lake[48]
VSi_2P_4	0.50	93.62	−6.84	3.83	0.00	−0.43	−0.43	−0.51	0.08	0.08	0.04	0.00	0.00	0.02	0.00	0.00	0.00	37.81	37.81	37.87	6-6-6-12	257.04	264.99	N/A, Akanda and Lake[48]
VTe_2-1T	0.63	−3.27	10.99	15.62	0.00	0.35	0.35	0.04	−1.51	−1.51	−0.92	−0.34	−0.34	−0.33	0.00	0.00	0.00	540.32	540.32	539.15	6-6-6-12	149.88	402.54	N/A
VTe_2-1T_refit	0.50	−5.11	17.18	24.41	0.00	0.55	0.55	0.06	−2.36	−2.36	−1.44	−0.53	−0.53	−0.51	0.00	0.00	0.00	844.32	844.32	842.48	6-6-6-12	150.00	152.57	N/A

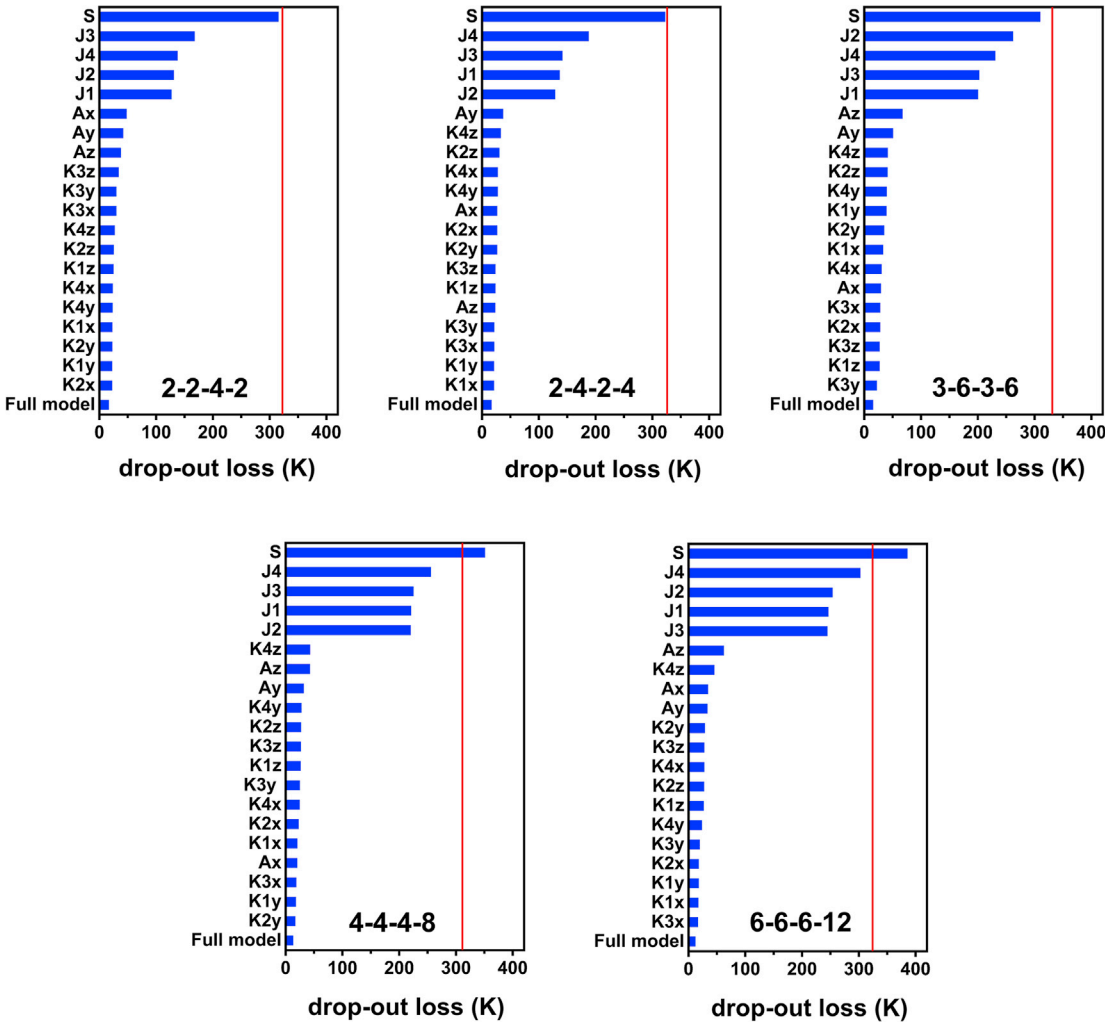

Figure 6. Permutation feature importance analysis of the models

The red vertical line indicates the baseline drop-out loss, i.e., the drop-out loss when all features are permutated together.

values of J_1 far exceed the training limit of 20 meV/link. A similar example can be seen for the case of refitted VTe_2-1T , where the values of A_d exceed the training limit of 300 meV/atom.

It is remarkable to note that the DFT-MC-based predictions listed in Table 1 have been obtained using the χ peak-based definition of T_C, whereas the ML model is trained with the data generated with our empirical magnetism-based definition. The close match between the two predictions reaffirms the correctness of the empirical definition.

Interpretability of the models

To draw physical insights from the models, next we perform a global interpretability analysis spanning the whole datasets. We select the permutation feature importance (PFI)[49,50] scheme as the ideal analysis tool for this kind of regression problem. Under this scheme, first, the original model error over the whole dataset is estimated: $e_{orig} = L(y, \hat{f}(X))$, where $\hat{f}$ is the trained model, X is the input feature matrix, y is the target vector containing the $T_{C\text{-}MC}$ values, and $L(y, \hat{f})$ is the loss function or error measure, which is chosen to be MAE here. Then for each feature q, a separate feature matrix X_{perm-q} is generated by randomly shuffling or permuting the feature column. This procedure breaks the association between the feature and the true target y. Next, the permutation error is estimated based on the predictions of the permuted data; $e_{perm-q} = L(y, \hat{f}(X_{perm-q}))$. Finally, the PFI for this feature is calculated as $PFI_q = e_{perm-q} - e_{orig}$. The PFI_q score is indicative of how much the model depends on the particular feature q. In Figure 6 we graphically represent the results of this analysis for all crystal types. For all the cases, the value of S proved to be the most important, followed by the J_p features (p = 1, 2, 3, 4), followed by the exchange and on-site anisotropy parameters. The higher importance of the isotropic exchanges compared with the anisotropy parameters can perhaps be guessed just by a manual inspection of the data, but the unanimous highest importance score of S is a surprise and perhaps originates from the fact that every term of the Hamiltonian is multiplied by the square of S. For the two most highly coordinated crystal types, 4-4-4-8 and 6-6-6-12, the importance of S seems to be more than that of all the features combined.

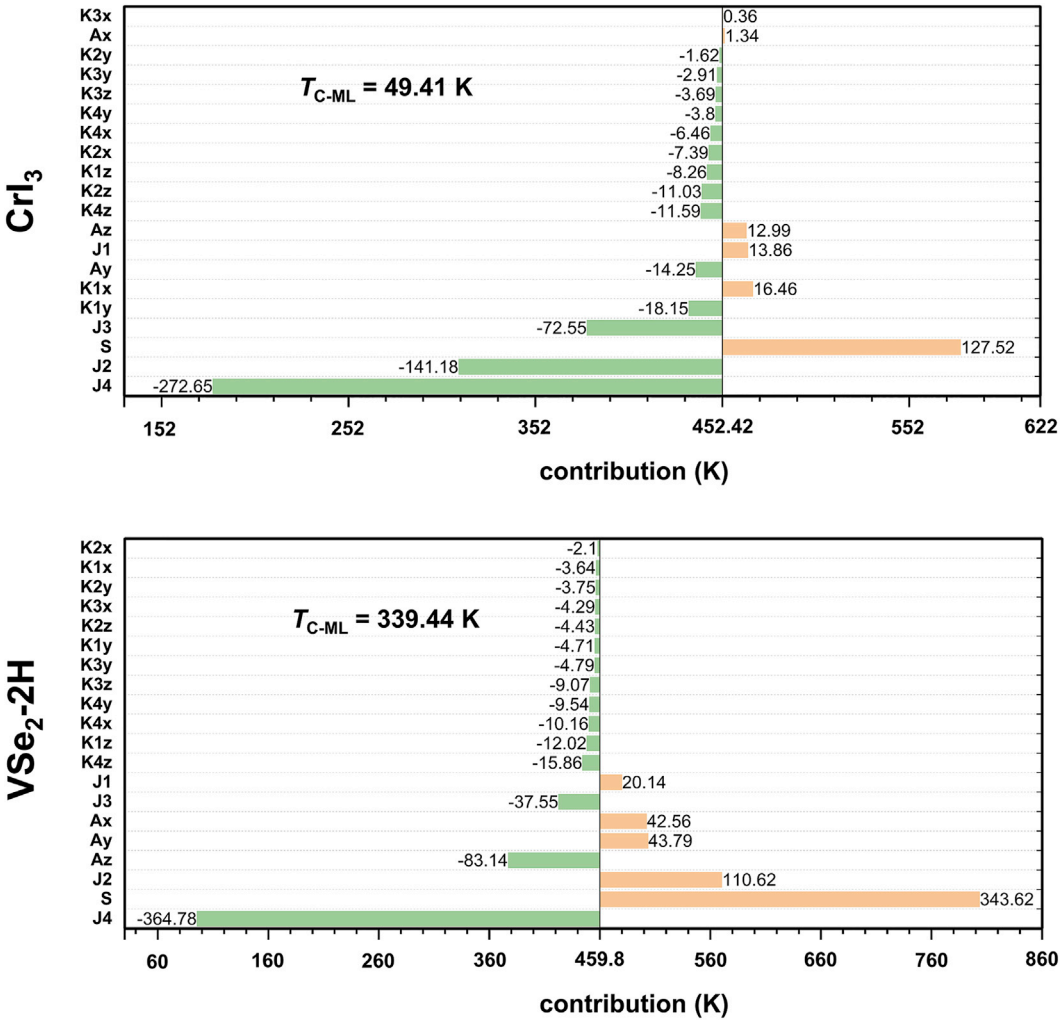

Figure 7. Shapley analysis of the ML models for two materials, CrI_3 and 2H VSe_2

For two real 2D FM materials, the first one perhaps being the most famous of them all, CrI_3 (crystal type 3-6-3-6),[1] and the second one being a high-temperature ferromagnet, 2H VSe_2 (crystal type 6-6-6-12),[6] we perform local interpretability analysis using Shapley scores. The scores with relevant context are pictorially illustrated in Figure 7. The Shapley method is a game-theory-based approach that, for a particular prediction, tells us which feature contributed how much to the process of arriving at the true prediction from the expected or average prediction of the model.[51,52] For the 3-6-3-6 model, the expected prediction value of the model is 452.42 K over the whole dataset, while the actual predicted value for CrI_3 is 49.41 K. We see that J_4 contributes the most to reach the actual value, a huge −272.65 K. This might seem somewhat surprising considering the J_4 value is 0 for CrI_3. The training data distribution can explain the origin of this apparent anomaly. While generating the inputs, we gave equal weight to all four J_p, as seen from the data distribution. In nature, however, the further one goes from the reference site, usually the less the effect of the exchange interaction should become. Unfortunately, we could not find a way to incorporate this effect into the input data. As a result, the 0 value of J_4 helps most in bringing down the mean prediction value to the actual value. The second-largest contribution comes from J_2, at −141.18 K. For CrI_3 the J_2 value is only 0.48 meV/link, and the enormous negative contribution can again be explained by the same logic. This is also the case for $J_3 = -0.04$ meV/link, contributing −72.55 K. Unsurprisingly, both $J_1 = 3.04$ meV/link and $S = 1.5$ contribute positively to raising the average prediction 13.86 K and 127.52 K.

For the 6-6-6-12 model, the expected prediction value is 459.8 K while the actual predicted value for 2H VSe_2 is 339.44 K. Like the previous case, here also a large negative contribution of $J_4 = 0$ and a large positive contribution of $S = 0.5$ is observed (−364.78 K and 343.62 K). The unusually strong negative $J_2 = -5.02$ meV/link contributes highly positively (110.62 K), while the out-of-training-range $J_1 = 141.99$ meV/link contributes mildly positively (20.14 K). We conclude that because of the large positive J_1 and large negative J_2 values, this becomes a peculiar case to interpret as the model overcompensates for these values with other features. However, it is remarkable that despite dealing with such out-of-range input, the prediction of the model remains exact.

It is worth mentioning that there have been attempts to build data-driven mean-field-like models to predict the values of T_C

of 2D FM materials, which rely on the assumption that T_C holds a linear relationship with quantities such as J_pS^2, $K_{p\sigma}S^2$, and $A_\sigma S^2$.[23] In our exhaustive experiment with a quarter of a million data points, however, we found absolutely no linear relationship between J_pS^2 and T_C, as depicted in the plots of Figure S6 for the typical case of 6-6-6-12, and thus conclude such linear models are not good enough to capture the complex relationship of T_C with the material parameters.

We have attempted to develop a "unified" single model for all crystal types. To this end, four additional features, CN_1, CN_2, CN_3, and CN_4, are added to the existing list of 20 input features because they succinctly carry the crystal structure information. However, despite an extensive model search and training, we were unable to find a model that could match the prediction accuracy of the models developed for individual crystal types. Perhaps data enrichment or augmentation with additional crystal features, training with more data, or combining both can improve the unified model's performance, but this is beyond the scope of this work. The same unified model can also be used to predict the T_C of any unknown crystal if the chosen crystal features are easy to calculate.

From our PFI analysis, it has been confirmed that the major players that determine the T_C of 2D materials are S and the J_p terms, while K_{pz} and A_z terms contribute minimally. Note that in the MC process, all terms, small or large, take up nearly equal time for the multiplication operations. Therefore, to produce a "quick" dataset for training the very first intermediate model, one can perhaps omit the anisotropy terms and still end up with a reasonable model. This does not make sense physically, as the anisotropy is solely responsible for lifting the Mermin-Wegner restriction in two dimensions, but instead can be used as a "numerical trick." Of course, for precise prediction of T_C, the anisotropy terms must be included in the MC process for subsequent batches.

As mentioned, the lack of data for training a reliable ML model is typical for materials science problems. Another problem can be highly skewed data similar to those of this work. Our developed concept of ML-guided data generation can be useful for these cases to obtain a near-uniform output distribution.

To summarize, in this work we have developed a DFT-MC-based automated computational pipeline that can accurately predict the transition temperatures of any 2D magnetic materials from its crystal structure without any empirical corrections. Continuing with the same spin Hamiltonian, we generate a quarter of a million hypothetical materials data by sampling the input space nearly uniformly and by performing a massive amount of MC simulations with this input set. ML models are trained on these data to build highly accurate T_C predictors that can perform the job of the computationally heavy MC process in the blink of an eye. The interpretability of these models is also explored. Our work might help scientists to discover high-temperature 2D magnets rapidly and with ease.

EXPERIMENTAL PROCEDURES

Resource availability

Lead contact

Requests for further information should be directed to and will be fulfilled by the lead contact, Santanu Mahapatra (santanu@iisc.ac.in).

Materials availability

This computational study did not generate any new unique reagents.

Data and code availability

The authors declare that the main data supporting the findings of this study are available within the paper and its supplemental files. Original data have been deposited to Figshare: https://doi.org/10.6084/m9.figshare.20439309. All the datasets and ML models are freely available here. Other relevant data are available from the lead contact upon reasonable request.

A rolling release of the developed automated python code for T_C or T_N prediction, e2e_v2, is available at https://github.com/arnabkabiraj/e2e_v2/. A frozen version of the code that can be used to reproduce the results presented in the paper is available at https://doi.org/10.5281/zenodo.7276466. The details about obtaining VASP, a proprietary code, can be found at https://www.vasp.at/.

DFT calculations

DFT calculations of this work are carried out using a meta-generalized gradient approximation (meta-GGA) as implemented in the code Vienna Ab Initio Simulation Package (VASP)[53–56] with the Projector-Augmented-Wave (PAW)[57] method using the r^{2}SCAN exchange-correlation functional.[32] The Materials Project[58] recommended pseudopotentials (https://docs.materialsproject.org/methodology/mof-methodology/calculation-parameters/psuedopotentials) have been used throughout. Sufficiently large cutoff energy of 520 eV is used to avoid Pulay stress. A gamma-centered k-points grid with reciprocal density 150 Å^{-3} is used to sample the Brillouin zone for all structural relaxations. A similar k-mesh with reciprocal density 300 Å^{-3} is employed for all static runs, including the non-collinear ones. Electronic convergence is set to be attained when the difference in energy of successive electronic steps becomes less than 10^{-6} eV, whereas the structural geometry is optimized until the maximum Hellmann-Feynman force on every atom falls below 0.01 eV/Å. A large vacuum space of 25 Å in the vertical direction is applied to avoid any spurious interaction between periodically repeated layers. All crystal structures are visualized using the tool VESTA.[59] The python libraries pymatgen (Python Materials Genomics) and custodian[60] have been used extensively in the high-throughput pipeline code to achieve full automation. The library Atomic Simulation Environment (ASE)[61] has also been used for some operations.

The automated workflow uses the MagneticStructureEnumerator class from the pymatgen.analysis.magnetism.analyzer module to generate the different spin configurations. For the different AFM configurations, this usually means making suitable supercells from the unit cell to accommodate the possible spin configurations. To locate the ground state, i.e., the most stable spin configuration, all of these configurations are fully relaxed, whereby both the atomic and lattice degrees of freedom are allowed to change. Once the ground state is identified, we only proceed further with that particular structure: a larger uniformly sized supercell is constructed from this structure which can accommodate all the spin configurations, and all static runs are performed on this supercell only, which ultimately provides us with the magnetic parameters of the material. To summarize, the supercells are relaxed only to locate the ground state, but all the static runs are performed on a supercell constructed from this ground state, only changing the spin directions. The rationale behind this choice is as follows: relaxing the supercells can often lead to additional energetic stability via undesired symmetry breaking,[62] or even digression towards a CDW ground state.[63] The FM state, however, is usually determined from the unit cell and therefore does not incorporate the effect of symmetry breaking in larger supercells. Thus, erroneous predictions of the magnetic parameters might ensue if the supercells are allowed to relax. On the other hand, the relaxation process to find the ground state includes the effect of symmetry breaking or CDW and establishes the state's superlative stability beyond doubt. If there is no significant energy gain via symmetry breaking or CDW transition, the effect of relaxing the structures to obtain the magnetic parameters is usually negligible. We test our workflow using the GGA + U methodology with the well-regarded values of U = 2.7 eV and J = 0.7 eV[64–66] (with the rotationally invariant DFT + U method introduced by Liechtenstein et al.[67]) for the materials CrI_3 and $CrBr_3$ and found the T_C to be 42 K and 24 K, respectively, extremely close to the experimental reports.[1,38]

One advantage of this choice is that if one is sure of the ground-state structure beforehand, they can simply relax the structure to this ground state once and then directly use this to find the magnetic parameters instead of relaxing all

the spin configurations. Our code allows this using input "relax_structures = False."

The different spin configurations (with the structural information of the ground state) and their collinear and non-collinear total energies for all the materials listed in Table 1 are provided in Data S1. Note that the magnetic moments of these spin configurations are taken directly from the VASP OUTCAR files, which only account for the magnetism in a sphere of a fixed radius (defined by the RWIGS tag) around the ionic positions and therefore might not always be accurate, as the volume of the magnetic ions might change with different spin configurations. However, these configurations can clearly be identified by the signs of the magnetic moments.

MC simulations

To study the FM-to-PM transition of the 2D materials, MC simulations of the aforementioned Hamiltonian have been performed using the Metropolis algorithm with the single-spin update scheme. A 64 × 64 supercell with in-plane periodic boundary conditions containing 4,096 magnetic sites has been used to simulate the 2D systems to eliminate the size effects. In total, 1.5×10^5 Monte Carlo steps (MCS) have been performed for each temperature while the results from the first 0.5×10^5 steps have been discarded, as the system is allowed to equilibrate or thermalize during this time. The final values of magnetization and susceptibility are calculated as the average over the last 10^5 MC steps for each temperature. The massive amount of MC simulations was performed parallelly on thousands of cores of a supercomputer, each core handling a different material at a time.

Machine learning

The selection of the training set plays a crucial role in the fitting of the ML model. The set should contain samples that are the best representation of the input space, making the training generalized and the training model closer to the actual function to be learned. The training data from a fully random test-train split might not fulfill this criterion. Here we have used the Latin Hypercube Sampling (LHS)[68] scheme to generate the training set with maximum representation. The idaes.surrogate.pysmo.sampling.LatinHypercubeSampling class from the IDAES Toolkit (https://github.com/IDAES/idaes-pse) has been used to generate the ≈45,000 samples for each crystal type. The models trained on the LHS-sampled data produce much better predictions on unseen test sets than the fully random splitting.

The DNN models were identified and trained using the autoML library AutoKeras (https://github.com/keras-team/autokeras).[69] Based on the performance on a validation set, AutoKeras automatically finds the best neural architecture and hyperparameters, such as the optimizer type, learning rate, and batch size, for training. After rigorous testing, the MAE was selected as the ideal loss function to be minimized, as it consistently outperformed other available loss functions in terms of validation set prediction. The last 20% of training data were kept as the validation set, which is the default for AutoKeras. The autokeras.StructuredDataRegressor class was used to find and train the models. The default values of 1,000 epochs and early stopping with patience equal to 30 are used for the fitting. The objective of fitting was to minimize the loss on the validation set. A maximum of 300 trials were performed. AutoKeras uses KerasTuner (https://github.com/keras-team/keras-tuner) as the hyperparameter optimizer backend, and the default values were used there as well.

For the interpretability analysis, the moDel Agnostic Language for Exploration and eXplanation or DALEX (https://github.com/ModelOriented/DALEX) package was used.[70] The whole datasets were fed to the dalex.Explainer class, and the model_parts method of this class was used to perform the PFI analyses. All data were sampled, and 20 permutation rounds were performed on each feature. The predict_parts method from the same class was used to obtain the Shapley scores. For each case, all data were sampled, a total of 50 random paths were explored, and the mean scores from all these paths were taken as the final Shapley scores.

SUPPLEMENTAL INFORMATION

Supplemental information can be found online at https://doi.org/10.1016/j.patter.2022.100625.

ACKNOWLEDGMENTS

The authors thank Supercomputer Education and Research Centre (SERC), Indian Institute of Science (IISc) Bangalore, for facilitating the CRAY XC40-SahasraT and Param Pravega (https://www.serc.iisc.ac.in/supercomputer/for-traditional-hpc-simulations-param-pravega/) supercomputers for performing the massive MC simulations. The computational charges were supported by the Core Research Grant (CRG) scheme of the Science and Engineering Research Board (SERB), Government of India, under grant no. CRG/2020/000758.

AUTHOR CONTRIBUTIONS

A.K. designed and implemented the automated computational workflow, developed the code e2e_v2, performed the DFT calculations and MC simulations, generated the datasets, and analyzed the results. T.J. developed the ML models. T.J. and A.K. performed the interpretability analyses. S.M. conceived the problem statement, designed the graphics, and supervised the overall work. A.K. and S.M. wrote the manuscript with input from T.J.

DECLARATION OF INTERESTS

The authors declare no competing interests.

INCLUSION AND DIVERSITY

We support inclusive, diverse, and equitable conduct of research.

Received: August 16, 2022
Revised: September 9, 2022
Accepted: October 11, 2022
Published: November 14, 2022

REFERENCES

1. Huang, B., Clark, G., Navarro-Moratalla, E., Klein, D.R., Cheng, R., Seyler, K.L., Zhong, D., Schmidgall, E., McGuire, M.A., Cobden, D.H., et al. (2017). Layer-dependent ferromagnetism in a van der Waals crystal down to the monolayer limit. Nature *546*, 270–273. https://doi.org/10.1038/nature22391.
2. Gong, C., Li, L., Li, Z., Ji, H., Stern, A., Xia, Y., Cao, T., Bao, W., Wang, C., Wang, Y., et al. (2017). Discovery of intrinsic ferromagnetism in two-dimensional van der Waals crystals. Nature *546*, 265–269. https://doi.org/10.1038/nature22060.
3. Lee, J.-U., Lee, S., Ryoo, J.H., Kang, S., Kim, T.Y., Kim, P., Park, C.-H., Park, J.-G., and Cheong, H. (2016). Ising-type magnetic ordering in atomically thin FePS3. Nano Lett. *16*, 7433–7438. https://doi.org/10.1021/acs.nanolett.6b03052.
4. Mermin, N.D., and Wagner, H. (1966). Absence of ferromagnetism or antiferromagnetism in one- or two-dimensional isotropic Heisenberg models. Phys. Rev. Lett. *17*, 1133–1136. https://doi.org/10.1103/PhysRevLett.17.1133.
5. Bonilla, M., Kolekar, S., Ma, Y., Diaz, H.C., Kalappattil, V., Das, R., Eggers, T., Gutierrez, H.R., Phan, M.-H., and Batzill, M. (2018). Strong room-temperature ferromagnetism in VSe2 monolayers on van der Waals substrates. Nat. Nanotechnol. *13*, 289–293. https://doi.org/10.1038/s41565-018-0063-9.
6. Wang, X., Li, D., Li, Z., Wu, C., Che, C.-M., Chen, G., and Cui, X. (2021). Ferromagnetism in 2D vanadium diselenide. ACS Nano *15*, 16236–16241. https://doi.org/10.1021/acsnano.1c05232.
7. O'Hara, D.J., Zhu, T., Trout, A.H., Ahmed, A.S., Luo, Y.K., Lee, C.H., Brenner, M.R., Rajan, S., Gupta, J.A., McComb, D.W., and Kawakami, R.K. (2018). Room temperature intrinsic ferromagnetism in epitaxial manganese selenide films in the monolayer limit. Nano Lett. *18*, 3125–3131. https://doi.org/10.1021/acs.nanolett.8b00683.

8. Feng, Y.P., Shen, L., Yang, M., Wang, A., Zeng, M., Wu, Q., Chintalapati, S., and Chang, C. (2017). Prospects of spintronics based on 2D materials. WIREs Comput. Mol. Sci. *7*, e1313. https://doi.org/10.1002/wcms.1313.

9. Farooq, M.U., and Hong, J. (2019). Switchable valley splitting by external electric field effect in graphene/CrI3 heterostructures. Npj 2D Mater. Appl. *3*, 3. https://doi.org/10.1038/s41699-019-0086-6.

10. Soumyanarayanan, A., Reyren, N., Fert, A., and Panagopoulos, C. (2016). Emergent phenomena induced by spin–orbit coupling at surfaces and interfaces. Nature *539*, 509–517. https://doi.org/10.1038/nature19820.

11. Guo, Y., Zhou, S., and Zhao, J. (2021). Two-dimensional intrinsic ferromagnets with high Curie temperatures: synthesis, physical properties and device applications. J. Mater. Chem. C *9*, 6103–6121. https://doi.org/10.1039/D1TC00415H.

12. Mhirech, A., Aouini, S., Alaoui-Ismaili, A., and Bahmad, L. (2017). Study of RKKY interactions in a bilayer graphene structure with non-equivalent planes. J. Supercond. Nov. Magn. *30*, 3189–3198. https://doi.org/10.1007/s10948-017-4146-x.

13. Mounet, N., Gibertini, M., Schwaller, P., Campi, D., Merkys, A., Marrazzo, A., Sohier, T., Castelli, I.E., Cepellotti, A., Pizzi, G., and Marzari, N. (2018). Two-dimensional materials from high-throughput computational exfoliation of experimentally known compounds. Nat. Nanotechnol. *13*, 246–252. https://doi.org/10.1038/s41565-017-0035-5.

14. Miao, N., Xu, B., Zhu, L., Zhou, J., and Sun, Z. (2018). 2D intrinsic ferromagnets from van der Waals antiferromagnets. J. Am. Chem. Soc. *140*, 2417–2420. https://doi.org/10.1021/jacs.7b12976.

15. Fadil, Z., Maaouni, N., Qajjour, M., Mhirech, A., Kabouchi, B., Bahmad, L., and Ousi Benomar, W. (2020). Magnetization and susceptibility behaviors in a bi-layer graphyne structure: a Monte Carlo study. Phys. B Condens. Matter *578*, 411852. https://doi.org/10.1016/j.physb.2019.411852.

16. Zhang, H. (2021). High-throughput design of magnetic materials. Electron. Struct. *3*, 033001. https://doi.org/10.1088/2516-1075/abbb25.

17. Wang, Q.H., Bedoya-Pinto, A., Blei, M., Dismukes, A.H., Hamo, A., Jenkins, S., Koperski, M., Liu, Y., Sun, Q.-C., Telford, E.J., et al. (2022). The magnetic genome of two-dimensional van der Waals materials. ACS Nano *16*, 6960–7079. https://doi.org/10.1021/acsnano.1c09150.

18. Torelli, D., and Olsen, T. (2018). Calculating critical temperatures for ferromagnetic order in two-dimensional materials. 2D Mater. *6*, 015028. https://doi.org/10.1088/2053-1583/aaf06d.

19. Kabiraj, A., Kumar, M., and Mahapatra, S. (2020). High-throughput discovery of high Curie point two-dimensional ferromagnetic materials. Npj Comput. Mater. *6*, 35. https://doi.org/10.1038/s41524-020-0300-2.

20. Torelli, D., Moustafa, H., Jacobsen, K.W., and Olsen, T. (2020). High-throughput computational screening for two-dimensional magnetic materials based on experimental databases of three-dimensional compounds. Npj Comput. Mater. *6*, 158. https://doi.org/10.1038/s41524-020-00428-x.

21. Liu, L., Lin, Z., Hu, J., and Zhang, X. (2021). Full quantum search for high T_c two-dimensional van der Waals ferromagnetic semiconductors. Nanoscale *13*, 8137–8145. https://doi.org/10.1039/D0NR08687H.

22. Tiwari, S., Vanherck, J., Van de Put, M.L., Vandenberghe, W.G., and Sorée, B. (2021). Computing Curie temperature of two-dimensional ferromagnets in the presence of exchange anisotropy. Phys. Rev. Res. *3*, 043024–43110. https://doi.org/10.1103/PhysRevResearch.3.043024.

23. Lu, X., Fei, R., and Yang, L. (2019). Curie temperature of emerging two-dimensional magnetic structures. Phys. Rev. B *100*, 205409. https://doi.org/10.1103/PhysRevB.100.205409.

24. Moore, G.C., Horton, M.K., Ganose, A.M., Siron, M., and Persson, K.A. (2022). High-throughput determination of Hubbard U and Hund J values for transition metal oxides via linear response formalism. Preprint at arXiv. https://doi.org/10.48550/arXiv.2201.04213.

25. Schmidt, J., Marques, M.R.G., Botti, S., and Marques, M.A.L. (2019). Recent advances and applications of machine learning in solid-state materials science. Npj Comput. Mater. *5*, 83. https://doi.org/10.1038/s41524-019-0221-0.

26. Prezhdo, O.V. (2020). Advancing physical chemistry with machine learning. J. Phys. Chem. Lett. *11*, 9656–9658. https://doi.org/10.1021/acs.jpclett.0c03130.

27. Périgo, E.A., and Faria, R.N.d. (2021). Artificial intelligence—engineering magnetic materials: current status and a brief perspective. Magnetochemistry *7*, 84. https://doi.org/10.3390/magnetochemistry7060084.

28. (2021). Rise of the machines. Nat. Rev. Mater. *6*, 641. https://doi.org/10.1038/s41578-021-00351-7.

29. Acosta, C.M., Ogoshi, E., Souza, J.A., and Dalpian, G.M. (2022). Machine learning study of the magnetic ordering in 2D materials. ACS Appl. Mater. Interfaces *14*, 9418–9432. https://doi.org/10.1021/acsami.1c21558.

30. Lu, S., Zhou, Q., Guo, Y., and Wang, J. (2022). On-the-fly interpretable machine learning for rapid discovery of two-dimensional ferromagnets with high Curie temperature. Chem *8*, 769–783. https://doi.org/10.1016/j.chempr.2021.11.009.

31. Shen, Z.-X., Su, C., and He, L. (2022). High-throughput computation and structure prototype analysis for two-dimensional ferromagnetic materials. Npj Comput. Mater. *8*, 132. https://doi.org/10.1038/s41524-022-00813-8.

32. Furness, J.W., Kaplan, A.D., Ning, J., Perdew, J.P., and Sun, J. (2020). Accurate and numerically efficient r^2 SCAN meta-generalized gradient approximation. J. Phys. Chem. Lett. *11*, 8208–8215. https://doi.org/10.1021/acs.jpclett.0c02405.

33. Torelli, D., Thygesen, K.S., and Olsen, T. (2019). High throughput computational screening for 2D ferromagnetic materials: the critical role of anisotropy and local correlations. 2D Mater. *6*, 045018. https://doi.org/10.1088/2053-1583/ab2c43.

34. Sun, J., Ruzsinszky, A., and Perdew, J.P. (2015). Strongly constrained and appropriately normed Semilocal density functional. Phys. Rev. Lett. *115*, 036402. https://doi.org/10.1103/PhysRevLett.115.036402.

35. Sun, J., Remsing, R.C., Zhang, Y., Sun, Z., Ruzsinszky, A., Peng, H., Yang, Z., Paul, A., Waghmare, U., Wu, X., et al. (2016). Accurate first-principles structures and energies of diversely bonded systems from an efficient density functional. Nat. Chem. *8*, 831–836. https://doi.org/10.1038/nchem.2535.

36. Chakraborty, A., Dixit, M., Aurbach, D., and Major, D.T. (2018). Predicting accurate cathode properties of layered oxide materials using the SCAN meta-GGA density functional. Npj Comput. Mater. *4*, 60. https://doi.org/10.1038/s41524-018-0117-4.

37. Devi, R., Singh, B., Canepa, P., and Sai Gautam, G. (2022). Effect of exchange-correlation functionals on the estimation of migration barriers in battery materials. Npj Comput. Mater. *8*, 160. https://doi.org/10.1038/s41524-022-00837-0.

38. Kim, H.H., Yang, B., Li, S., Jiang, S., Jin, C., Tao, Z., Nichols, G., Sfigakis, F., Zhong, S., Li, C., et al. (2019). Evolution of interlayer and intralayer magnetism in three atomically thin chromium trihalides. Proc. Natl. Acad. Sci. USA *116*, 11131–11136. https://doi.org/10.1073/pnas.1902100116.

39. Zhang, Z., Shang, J., Jiang, C., Rasmita, A., Gao, W., and Yu, T. (2019). Direct photoluminescence probing of ferromagnetism in monolayer two-dimensional $CrBr_3$. Nano Lett. *19*, 3138–3142. https://doi.org/10.1021/acs.nanolett.9b00553.

40. Cai, X., Song, T., Wilson, N.P., Clark, G., He, M., Zhang, X., Taniguchi, T., Watanabe, K., Yao, W., Xiao, D., et al. (2019). Atomically thin $CrCl_3$: an in-plane layered antiferromagnetic insulator. Nano Lett. *19*, 3993–3998. https://doi.org/10.1021/acs.nanolett.9b01317.

41. Zhang, Y., and Ling, C. (2018). A strategy to apply machine learning to small datasets in materials science. Npj Comput. Mater. *4*, 25. https://doi.org/10.1038/s41524-018-0081-z.

42. Kabiraj, A., and Mahapatra, S. (2020). Intercalation-driven reversible switching of 2D magnetism. J. Phys. Chem. C *124*, 1146–1157. https://doi.org/10.1021/acs.jpcc.9b09477.

43. Meng, L., Zhou, Z., Xu, M., Yang, S., Si, K., Liu, L., Wang, X., Jiang, H., Li, B., Qin, P., et al. (2021). Anomalous thickness dependence of Curie temperature in air-stable two-dimensional ferromagnetic 1T-CrTe2 grown by

chemical vapor deposition. Nat. Commun. *12*, 809. https://doi.org/10.1038/s41467-021-21072-z.

44. Son, J., Son, S., Park, P., Kim, M., Tao, Z., Oh, J., Lee, T., Lee, S., Kim, J., Zhang, K., et al. (2021). Air-stable and layer-dependent ferromagnetism in atomically thin van der Waals $CrPS_4$. ACS Nano *15*, 16904–16912. https://doi.org/10.1021/acsnano.1c07860.
45. Deng, J., Guo, J., Hosono, H., Ying, T., and Chen, X. (2021). Two-dimensional bipolar ferromagnetic semiconductors from layered antiferromagnets. Phys. Rev. Mater. *5*, 034005. https://doi.org/10.1103/PhysRevMaterials.5.034005.
46. Lee, K., Dismukes, A.H., Telford, E.J., Wiscons, R.A., Wang, J., Xu, X., Nuckolls, C., Dean, C.R., Roy, X., and Zhu, X. (2021). Magnetic order and symmetry in the 2D semiconductor CrSBr. Nano Lett. *21*, 3511–3517. https://doi.org/10.1021/acs.nanolett.1c00219.
47. Wang, H., Qi, J., and Qian, X. (2020). Electrically tunable high Curie temperature two-dimensional ferromagnetism in van der Waals layered crystals. Appl. Phys. Lett. *117*, 083102. https://doi.org/10.1063/5.0014865.
48. Akanda, M.R.K., and Lake, R.K. (2021). Magnetic properties of $NbSi_2N_4$, VSi_2N_4, and VSi_2P_4 monolayers. Appl. Phys. Lett. *119*, 052402. https://doi.org/10.1063/5.0055878.
49. Breiman, L. (2001). Random Forests. Mach. Learn. *45*, 5–32. https://doi.org/10.1023/A:1010933404324.
50. Fisher, A., Rudin, C., and Dominici, F. (2019). All models are wrong, but many are useful: learning a variable's importance by studying an entire class of prediction models Simultaneously. J. Mach. Learn. Res. *20* (177), 1–81. https://jmlr.org/papers/v20/18-760.html.
51. Shapley, L.S. (1953). 17. A value for n-person games. In Contributions to the Theory of Games (AM-28), Volume II, Harold William Kuhn and Albert William Tucker, eds. (Princeton University Press), pp. 307–318. https://doi.org/10.1515/9781400881970-018.
52. Sundararajan, M., and Najmi, A. (2020). The many shapley values for model explanation. In Proceedings of the 37th International Conference on Machine Learning, *119*, Hal Daumé, III and Aarti Singh, eds. (PMLR), pp. 9269–9278. https://proceedings.mlr.press/v119/sundararajan20b.html.
53. Kresse, G., and Hafner, J. (1993). Ab initio molecular dynamics for liquid metals. Phys. Rev. B Condens. Matter *47*, 558–561. https://doi.org/10.1103/PhysRevB.47.558.
54. Kresse, G., and Hafner, J. (1994). Ab initio molecular-dynamics simulation of the liquid-metal–amorphous-semiconductor transition in germanium. Phys. Rev. B Condens. Matter *49*, 14251–14269. https://doi.org/10.1103/PhysRevB.49.14251.
55. Kresse, G., and Furthmüller, J. (1996). Efficient iterative schemes for ab initio total-energy calculations using a plane-wave basis set. Phys. Rev. B Condens. Matter *54*, 11169–11186. https://doi.org/10.1103/PhysRevB.54.11169.
56. Kresse, G., and Furthmüller, J. (1996). Efficiency of ab-initio total energy calculations for metals and semiconductors using a plane-wave basis set. Comput. Mater. Sci. *6*, 15–50. https://doi.org/10.1016/0927-0256(96)00008-0.
57. Kresse, G., and Joubert, D. (1999). From ultrasoft pseudopotentials to the projector augmented-wave method. Phys. Rev. B *59*, 1758–1775. https://doi.org/10.1103/PhysRevB.59.1758.
58. Jain, A., Ong, S.P., Hautier, G., Chen, W., Richards, W.D., Dacek, S., Cholia, S., Gunter, D., Skinner, D., Ceder, G., and Persson, K.A. (2013). Commentary: the materials project: a materials genome approach to accelerating materials innovation. Apl. Mater. *1*, 011002. https://doi.org/10.1063/1.4812323.
59. Momma, K., and Izumi, F. (2011). *VESTA 3* for three-dimensional visualization of crystal, volumetric and morphology data. J. Appl. Crystallogr. *44*, 1272–1276. https://doi.org/10.1107/S0021889811038970.
60. Ong, S.P., Richards, W.D., Jain, A., Hautier, G., Kocher, M., Cholia, S., Gunter, D., Chevrier, V.L., Persson, K.A., and Ceder, G. (2013). Python Materials Genomics (pymatgen): a robust, open-source python library for materials analysis. Comput. Mater. Sci. *68*, 314–319. https://doi.org/10.1016/j.commatsci.2012.10.028.
61. Hjorth Larsen, A., Jørgen Mortensen, J., Blomqvist, J., Castelli, I.E., Christensen, R., Dułak, M., Friis, J., Groves, M.N., Hammer, B., Hargus, C., et al. (2017). The atomic simulation environment—a Python library for working with atoms. J. Phys. Condens. Matter *29*, 273002. https://doi.org/10.1088/1361-648x/aa680e.
62. Liu, L., Chen, S., Lin, Z., and Zhang, X. (2020). A symmetry-breaking phase in two-dimensional FeTe2 with ferromagnetism above room temperature. J. Phys. Chem. Lett. *11*, 7893–7900. https://doi.org/10.1021/acs.jpclett.0c01911.
63. Kabiraj, A., and Mahapatra, S. (2020). Machine-intelligence-driven high-throughput prediction of 2D charge density wave phases. J. Phys. Chem. Lett. *11*, 6291–6298. https://doi.org/10.1021/acs.jpclett.0c01846.
64. Lado, J.L., and Fern'ndez-Rossier, J. (2017). On the origin of magnetic anisotropy in two dimensional CrI_3. 2D Mater. *4*, 035002. https://doi.org/10.1088/2053-1583/aa75ed.
65. Webster, L., and Yan, J.-A. (2018). Strain-tunable magnetic anisotropy in monolayer $CrCl_3$, $CrBr_3$, and CrI_3. Phys. Rev. B *98*, 144411. https://doi.org/10.1103/PhysRevB.98.144411.
66. Wu, Z., Yu, J., and Yuan, S. (2019). Strain-tunable magnetic and electronic properties of monolayer CrI3. Phys. Chem. Chem. Phys. *21*, 7750–7755. https://doi.org/10.1039/C8CP07067A.
67. Liechtenstein, A.I., Anisimov, V.I., and Zaanen, J. (1995). Density-functional theory and strong interactions: orbital ordering in Mott-Hubbard insulators. Phys. Rev. B Condens. Matter *52*, R5467–R5470. https://doi.org/10.1103/PhysRevB.52.R5467.
68. Swiler, L., Slepoy, R., and Giunta, A. (2006). Evaluation of sampling methods in constructing Response Surface approximations. In 47th AIAA/ASME/ASCE/AHS/ASC Structures, Structural Dynamics, and Materials Conference (Reston, VA, USA: American Institute of Aeronautics and Astronautics), pp. 1827–1851. https://doi.org/10.2514/6.2006-1827.
69. Jin, H., Song, Q., and Hu, X. (2019). Auto-keras: an efficient neural architecture search system. In Proceedings of the 25th ACM SIGKDD International Conference on Knowledge Discovery & Data Mining KDD '19 (Association for Computing Machinery), pp. 1946–1956. https://doi.org/10.1145/3292500.3330648.
70. Baniecki, H., Kretowicz, W., Piątyszek, P., Wiśniewski, J., and Biecek, P. (2021). Dalex: responsible machine learning with interactive explainability and fairness in python. J. Mach. Learn. Res. *22* (214), 1–7. https://www.jmlr.org/papers/v22/20-1473.html.